

Journal of Materials Chemistry A

Accepted Manuscript



This is an *Accepted Manuscript*, which has been through the Royal Society of Chemistry peer review process and has been accepted for publication.

Accepted Manuscripts are published online shortly after acceptance, before technical editing, formatting and proof reading. Using this free service, authors can make their results available to the community, in citable form, before we publish the edited article. We will replace this *Accepted Manuscript* with the edited and formatted *Advance Article* as soon as it is available.

You can find more information about *Accepted Manuscripts* in the [Information for Authors](#).

Please note that technical editing may introduce minor changes to the text and/or graphics, which may alter content. The journal's standard [Terms & Conditions](#) and the [Ethical guidelines](#) still apply. In no event shall the Royal Society of Chemistry be held responsible for any errors or omissions in this *Accepted Manuscript* or any consequences arising from the use of any information it contains.

Cite this: DOI: 10.1039/c0xx00000x

www.rsc.org/xxxxxx

ARTICLE TYPE

Bio-inspired Beehive-like Hierarchical Nanoporous Carbon Derived from Bamboo-based Industrial Byproduct as High Performance Supercapacitor Electrode Material

Weiqian Tian,^a Qiuming Gao,^{a*} Yanli Tan,^a Kai Yang,^a Lihua Zhu,^a Chunxiao Yang^a and Hang Zhang^a⁵ Received (in XXX, XXX) Xth XXXXXXXXX 20XX, Accepted Xth XXXXXXXXX 20XX

DOI: 10.1039/b000000x

Bio-inspired beehive-like hierarchical nanoporous carbon (BHNC) with a high specific surface area of 1472 m² g⁻¹ and a good electronic conductivity of 4.5 S cm⁻¹ is synthesized by carbonizing the industrial waste of bamboo-based byproduct. The BHNC sample exhibits remarkable electrochemical performances as supercapacitor electrode material such as high specific capacitance of 301 F g⁻¹ at 0.1 A g⁻¹ still maintaining that of 192 F g⁻¹ at 100 A g⁻¹, negligible capacitance loss after 20,000 cycles at 1 A g⁻¹, and high power density of 26,000 W kg⁻¹ at energy density of 6.1 Wh kg⁻¹ based on active electrode materials in aqueous electrolyte system. Moreover, an enhanced power density of 42,000 W kg⁻¹ at high energy density of 43.3 Wh kg⁻¹ is obtained in ionic liquid electrolyte system, which places the BHNC-based supercapacitors in the Ragone chart among the best energy-power synergetic outputting properties in ever reported for carbon-based supercapacitors.

Introduction

Stemmed from the climate change and depletion of fossil fuels, the market of green and sustainable energy storage systems (ESSs) with highly efficient, environmentally benign and low-cost characters are colossally increased.¹⁻⁴ Among these ESSs, electrochemical capacitors (supercapacitors) have been attracting intense research interest lately and are widely applied in the portable electronics and hybrid electric vehicles,^{5, 6} owing to their fascinating performances such as high power density, good cyclic stability, fast charge/discharge processes and low maintenance.^{7, 8} The electrochemical performance of an ideal supercapacitor with excellent energy-power combination properties is highly determined by the adopted active electrode materials and electrolyte. At a given electrolyte, the design and optimal nano-morphology of the active electrode materials for the best equilibrium between energy and power properties is still a significant goal because of the energy and power characteristics

competing with each other.⁹ Carbonaceous nanomaterials, such as nanoporous carbons and graphene, are the most common active electrode materials for supercapacitors owing to the tunable morphologies in nanosize, large specific surface areas, good conductivities and high chemical stability.^{10, 11} Graphene-based nanomaterials have been emerging as a new class of the ideal electrode candidates, such as curved/crumpled graphene,^{12, 13} microwave-exfoliated graphene,¹⁴ laser-scribed graphene,⁸ liquid electrolyte-mediated graphene¹⁵ and functionalized graphene.¹⁶ However, the produced cost of graphene-based nanomaterial is much more expensive than that of the nanoporous carbons derived from pyrolysis/hydrothermal of biomass,⁶ and the graphite from mineral deposits as main raw materials preparing graphene is very limited and will face the depletion with the prospective huge utilization on graphite-based electrode materials.¹⁷

Bio-inspired porous carbon materials derived from biomass resources are renewable/eco-friendly and rapidly increasing interest for supercapacitor electrode materials, such as direct

pyrolysis of seaweeds,^{18, 19} egg whites and eggshell membranes,²⁰⁻²² dead leaves,¹¹ human hairs²³ and pistachio nutshells,²⁴ and hydrothermal carbonization of eucalyptus wood sawdusts,²⁵ pollens,²⁶ corn cobs and spruces²⁷ and hemp.⁶ These carbon-based nanomaterials possess not only in regard to sustainable/economic advantages, but also in terms of the high specific surface area, rational average pore sizes and the optimal pore size distributions leading to high energy storage capabilities.^{9, 10} Based on sufficiently understanding the effect of pore size and surface area, a high capacitance can be obtained even at moderate specific surface area of about 1500 m² g⁻¹ by properly tailoring the pore sizes.¹¹ The ideal narrow pore size distribution consisting of most smaller than 1 nm but exactly matching with the size of bare (desolvated) electrolyte ions, such as EMIM⁺ of 0.43 nm and TFSI⁻ of 0.29 nm,²⁸ could lead to significant enhancement of specific capacitance (*C*),^{25, 28} since the substantial electrolyte ions are extruded through the micropores under a given potential and meanwhile the distance (*d*) of electrolyte ion center to pore wall is also decreased, extremely agreed with the equation $C = \epsilon A/d$ where ϵ is dielectric permittivity of electrolyte and *A* is surface area.^{29, 30} Compared to the reported metal carbide-derived carbon,²⁹⁻³¹ zeolite-templated micropore carbon,³² and nanoporous carbons synthesized from chemical polymers such as potassium citrate,¹⁰ ploy(acrylamide-co-acrylic acid) potassium,³³ the synthesis of novel nanoporous carbons from natural biomass with rational design of specific surface area, average pore size and pore size distribution is a toxic-free, low-cost and dominant research field.

Natural bamboo (*Phyllostachys pubescens*) is an eco-friendly, widely distributed and multifunctional plant. Currently, a mass of bamboo can be used as the raw materials to extract bioactive substances for medicinal applications such as di-*C*, *C*-hexosylapigenin, *O*-Hexosyl-*O*-deoxyhexosyl tricin, and 6-*C*-glucosylapigenin with high antioxidation, antibacterial, melanin inhibition, and antiallergic activities.^{34, 35} Large quantities of bamboo-based industrial byproducts of extraction residues are generated during the process (Fig. S1), waiting for value-added secondary-utilization as green energy storage materials. Here we have successfully prepared a novel bio-inspired beehive-like hierarchical nanoporous carbon (BHNC) employing bamboo-based industrial byproduct as a model carbon precursor by a simple and scalable combined process of hydrothermal carbonization, activation and vacuum annealing. The resulting BHNC sample with high specific surface area and good electronic conductivity renders a remarkable electrochemical performance as supercapacitor electrode material.

Experimental

Chemical

The bamboo (*Phyllostachys pubescens*)-based industrial byproduct used in the experiments were obtained from Yunnan province of China. 1-ethyl-3-methylimidazolium bis(trifluoromethylsulfonyl)imide (EMIM TFSI) and 1-butyl-1-methylpyrrolidinium bis(trifluoromethylsulfonyl) imide (BMPY TFSI) were purchased from Sigma-Aldrich. Potassium hydroxide, *N*-methyl-2-pyrrolidone (NMP) and all others reagents were purchased from Beijing Chemical Works, unless otherwise

specified and were used without further purification.

Synthesis of the material

2.0 g of bamboo-based industrial byproduct was uniformly dispersed in 40 mL of distilled water containing 0.5 mL of sulfuric acid through ultrasound. The dispersion was placed in a 100 mL stainless steel autoclave and was heated up to 200°C for 12 h and then allowed to cool to room temperature. The resulting solid product (hydrochar) was recovered by filtration, washed with distilled water and dried overnight at 80°C. The hydrochar was activated using KOH at a mass ratio of 1:1 (hydrochar/KOH) mixed in an agate mortar and heated at 800°C for 1 h under argon flow with a heating rate of 5°C min⁻¹ in a horizontal tubular oven. Finally, the samples were sufficiently washed with 10 vol% acetic acid solution to remove the residual inorganic impurities and then plenty of distilled water, followed by drying in an oven at 120°C for 5 h and annealed at 800°C for 1 h in a vacuum. In order to demonstrate the effect of the vacuum annealing, the control samples with unannealed (no 800°C in vacuum) process and annealing at 1000°C out the oxygen groups from the carbon surface were prepared, respectively, with other procedures as same as that of BHNC. To examine the effect of hydrothermal treatment to the morphology and porous structure of samples, another control sample was synthesized by direct pyrolysis of the bamboo-based industrial byproduct at 800°C for 2 h before the activation process.

Structural characterization

The composition of bamboo-based industrial byproduct was carried out by high-performance anion exchange chromatography (HPAEC) system (ICS-3000, Dionex). The morphologies and microstructures of the samples were observed by a field emission scanning electron microscopy (FE-SEM, JSM-7500F), transmission electron microscopy (TEM, JEM-2100) and high-resolution transmission electron microscopy (HR-TEM, JEM-2100F). Powder X-ray diffraction (XRD) patterns were determined by using an X-ray diffractometer (X-6000) with Cu K α radiation ($\lambda = 1.5406 \text{ \AA}$). Raman spectra were performed by a microscopic confocal Raman spectrometer (LabRAM HR800) at a laser wavelength of 514 nm. The electrical conductivity of the BHNC powders was determined in a four-point probe method (Jandel RM3) by pressing the powders at a pressure of 10 MPa. The porous texture characters of the samples were measured by the nitrogen sorption isotherms at 77 K (Micromeritics ASAP 2010), and the specific surface area and pore size distributions were analyzed by using the Brumauer-Emmett-Teller (BET) method and Non-Local Density Functional Theory (NLDFT) model using slit model. The surface elemental compositions were determined by X-ray photoelectron spectroscopy (XPS, Escalab 250) and infrared spectrometer (IR, iN10MX).

Electrochemical measurements in 6 M KOH

The aqueous supercapacitor performance was tested in 6 M KOH in three-electrode configuration and two-electrode symmetric cell. The work electrode was prepared that a slurry of 90% BHNC, 5% conducting carbon (Super-P) and 5% binder (PVDF) in NMP was pressed onto a nickel foam at 15 MPa and then dried at 100°C overnight in vacuum oven with a loading of about 2 mg cm⁻². A platinum foil and an Ag/AgCl electrode were used as the counter

and reference electrode in the three-electrode configuration, respectively. Cyclic voltammetry (CV) and galvanostatic charge-discharge curves were obtained on a CHI660D electrochemical workstation. The specific capacitance is calculated by $It/m\Delta E$ based on the charge-discharge curves in the three-electrode configuration, where I (A) is the discharge current, t (s) is the discharge time, m (g) is the mass of active electrode material, and ΔE (V) is the potential window. For the two-electrode symmetric supercapacitors, the devices were assembled by which two electrodes were separated by a porous polypropylene membrane soaked in 6 M KOH in CR2025-type coin cells. A CT2001E Battery Program Controlling Test System was used to measure the galvanostatic charge-discharge and the specific capacitance C was calculated by $2It/m\Delta E$, where m (g) is the active material weight of one electrode.

Electrochemical measurements in neat EMIM TFSI

To measure the non-aqueous symmetric supercapacitor performance in an neat ionic liquid of EMIM TFSI as electrolyte, the electrodes were prepared by pressing the above slurry containing the BHNC sample onto a conducting carbon substrate with a loading of about 5 mg cm^{-2} . Two electrodes were separated by a porous polypropylene membrane soaked in neat EMIM TFSI in CR2025-type coin cells. The CV curves were obtained on a CHI660D electrochemical workstation and the galvanostatic charge-discharge was measured at the CT2001E Battery Program Controlling Test System over a voltage window 3.5 V tested at 60°C . Electrochemical impedance spectroscopy (EIS) was tested at an open-circuit potential with the perturbation amplitude of 5 mV. For the symmetrical supercapacitors, the energy density E (Wh kg^{-1}) was calculated by $CV^2/(8 \times 3.6)$ and the power density P (W kg^{-1}) was calculated from E/t , where V (V) was the discharge voltage and t (h) is discharge time.

Results and discussion

Figure 1a illustrates the strategy of preparation approach for the BHNC sample from the bamboo-based industrial byproduct by combined processes of hydrothermal carbonization, activation and vacuum annealing. The bamboo-based industrial byproduct which originates from the bioactive-substance extraction residues as a model carbon precursor, comprises about 43.44 wt% cellulose (as glucan), 27.52 wt% lignin and 29.56 wt% hemicelluloses (28.42 wt% xylan, 0.83 wt% arabian and 0.31 wt% galactan) based on the high-performance anion exchange chromatography (HPAEC) analyses. The hydrothermal treatment to prepare hydrochar caused the feedstock to carbonization, self-assembled into nano-fragments and generation of no-open bottleneck macro/mesopores.^{25, 36} The resulting hydrochar owns uniform oxygen-containing groups.²² Then the succeeding activation using potassium hydroxide led to the formation of potassium carbonate by reacting with the oxygen-containing groups and carbon of hydrochar. These inorganic products were removed through acid and water washing to create micropores on the no-open meso/macropore walls. This process plays a crucial role to improve the available specific surface area and micropore porosity. Finally, the vacuum annealing resulted in further graphitization and thus improved the conductivity of samples.

The morphology and microstructure of the BHNC sample were

characterized by FESEM. The representative FESEM micrograph (Fig. 1b) clearly manifests that the BHNC owns the interconnected carbon nanosheet frameworks. The magnified FESEM image (Fig. 1c) suggests the existence of abundant pores in the interconnected carbon nanosheet frameworks. The high-magnification FESEM (Fig. 1d) indicates that the BHNC possesses a beehive-like hierarchical nanoporous structure on the interconnected carbon nanosheet frameworks, where the slits or cylindrical micropores are developed on the bottleneck-like meso/macropore walls leading to a hierarchical porous network, which is further demonstrated by the TEM image (Fig. 1e). The HR-TEM image (Fig. 1f) confirms the partial graphitization observed from the distorted lattice fringe images of the BHNC sample.

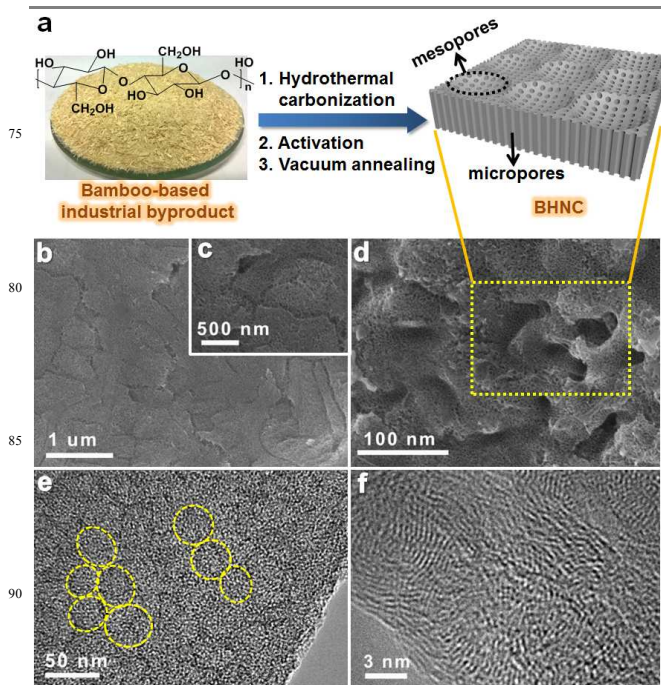


Fig. 1 (a) Schematic synthesis procedures of the BHNC sample with beehive-like hierarchical nanoporous structures, where the micropores were formed on the meso/macropores walls of the interconnected carbon nanosheet frameworks, (b-d) FESEM and (e) TEM images of the beehive-like microstructures of the BHNC sample, and (f) HR-TEM image of the edge of the BHNC. The beehive-like hierarchical nanoporous carbon framework could be clearly showed with the structural model shown in (a) and demonstrated by in (b-d) and the yellow rings in (e). The partial graphitization could be found from the distorted lattice fringe images in (f) of the BHNC.

The carbonization and graphitization degree of the BHNC sample was characterized by the XRD pattern (Fig. 2a). It can be clearly observed that the BHNC possesses two peaks which are consistent with graphitic carbon, albeit with incomplete. The broad peak at around 22° corresponds to the (002) reflection of the graphitic stacking, and the weak peak at about 43° which is the superposition of the (100) and (101) reflections, *i.e.*, (10) reflection, originates from the interlayer condensation and efficiently enhances the conductivity.^{23, 24} The Raman spectrum

(Fig. 2b) also shows two peaks around 1340 cm^{-1} (D-band) and 1590 cm^{-1} (G-band). The G-band peak at 1590 cm^{-1} stemmed from E_{2g} phonon vibrations of sp^2 -bonded carbon atoms is a characteristic feature of graphite layers, and the D-band peak at 1320 cm^{-1} attributed to the breathing mode of κ -point phonons with A_{1g} symmetry is related to the defective graphitic structure and disordered carbon (sp^3 -rich phase).^{33, 37} The intensity ratio (I_G/I_D) depended on the degree of graphitic structure,²¹ is 1.01 which is obviously higher than that of the commercial activated carbon (0.52).⁶ The BHNC sample also exhibits a large graphitic domain size of 4.04 nm calculated from the I_G/I_D .⁶ These observations from HR-TEM, XRD and Raman analyses further suggest that the BHNC owns partial graphitization structure leading to a good electronic conductivity of the samples. The electronic conductivity of the BHNC measured by a four-probed method is 4.5 S cm^{-1} at a pressure of 10 MPa , which is well comparable with that of the commercial activated carbon (super 50) of 4.3 S cm^{-1} for supercapacitors¹⁰ and higher than that of the reported carbon nanosheets derived from hemp ($2.1\text{--}2.3\text{ S cm}^{-1}$).⁶ While the control sample with the unannealed process show the lower electronic conductivity of 2.9 S cm^{-1} . The good electronic conductivity of BHNC can be attributed to the post-synthesis vacuum annealing of high temperature, and the high cellulose contents of bamboo fibers from the HPAEC analyses which can form the order structures during this approach.

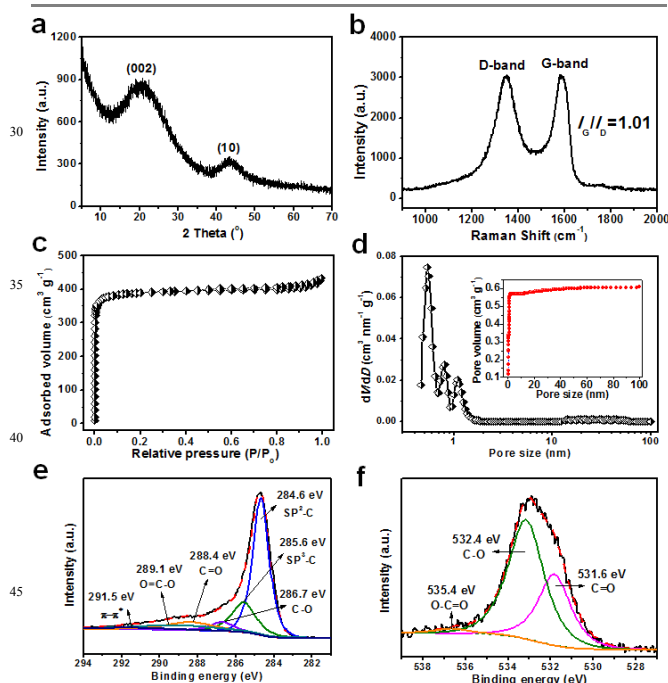


Fig. 2 (a) XRD pattern, (b) Raman spectrum, (c) Nitrogen adsorption-desorption isotherm with (d) the pore size distributions as well as (e) C1s and (f) O1s XPS spectra of the BHNC sample. Insert of (d) is the cumulative pore volume deduced by the NLDFT method.

The porous texture of the BHNC was measured by nitrogen adsorption-desorption at 77 K . Figure 2c shows that the BHNC exhibits a type-I isotherm with a sharp adsorption knee at low relative pressures and well-developed plateaus, indicating that it

is a typical microporous material and owns a narrow pore size distribution. The specific surface area of $1472\text{ m}^2\text{ g}^{-1}$ based on the standard BET method suggests that the BHNC is suitable as a supercapacitor electrode material. The pore size distributions calculated by the NLDFT model show hierarchical pore structures with three narrow micropore systems and a wide meso/macropore system (Fig. 2d). Most pore diameters are less than 1.5 nm consisted by three narrow micropore systems mainly around 0.54 nm and small part at about 0.79 nm and 1.09 nm . While a small fraction of meso/macropores with a wide pore diameter range from $10\text{--}60\text{ nm}$ may originate from the bottleneck-like pores. The pore volume distribution is shown in Figure 2d. The total pore volume is $0.61\text{ cm}^3\text{ g}^{-1}$ and above 79% pore volume is attributed to micropores. The moderate pore size distribution and total pore volume lead to a rational density of the BHNC (0.56 g cm^{-3}) higher than that of the commercial activated carbons, which are beneficial to improve the volumetric energy and power characteristics of the BHNC-based supercapacitors.

The chemical composition of the BHNC sample was determined by XPS. The XPS data suggest that the material contains $94.56\text{ mol}\%$ carbon, $4.79\text{ mol}\%$ oxygen and a small amount of $0.65\text{ mol}\%$ nitrogen. The XPS C1s spectrum (Fig. 2e) exhibits mainly single peak consisting of sp^2 -bonded carbon (284.6 eV) with a small tail containing sp^3 -bonded carbon (285.6 eV), C-O (286.7 eV), C=O (288.4 eV), O=C-O (289.1 eV) and a satellite peak of $\pi\rightarrow\pi^*$ (291.5 eV) at the higher-binding energy region,^{38–40} which indicates the formation of the abundant conjugated systems to improve its conductivity. The XPS O1s spectra (Fig. 2f) can be de-convoluted by three peaks representing C=O (531.6 eV), C-O (532.4 eV) and O=C=O (535.4 eV). These results are further demonstrated by the IR analysis (Fig. S2). The oxygen-containing groups and a small amount of nitrogen on the material surface can enhance the wettability of the electrodes with the electrolytes,^{18, 33} and the electron-rich nitrogen can also enhance the conductivity of the carbon materials.^{20, 23, 41} Moreover, these surface heteroatom-doped functional groups can act as the active sites for the additional pseudocapacitance leading to an enhanced electrochemical performance of BHNC as supercapacitor electrode.^{15–20}

Electrochemical performance

The BHNC-based aqueous supercapacitors were measured in both three-electrode configuration and two-electrode symmetric cell in 6 M KOH solution as electrolyte at the potential window of 1 V . To understand the intrinsic electrochemical behavior of the BHNC, the CV curves were recorded at different scan rates from 2 to 400 mV s^{-1} (Fig. 3a). It can be seen that the CV curves maintain an almost symmetric rectangular shape with weak-broadened humps even at high scan rate of 400 mV s^{-1} , indicating a dominant electric double-layer capacitance behavior with a strong synergistic effect of reversible pseudocapacitance from limited surface oxygen groups ($4.79\text{ mol}\%$ oxygen) including C=O/C-O as supported by XPS.^{15, 16}

In order to further confirm the unique beehive-like nanoporous structure of BHNC contribution to the electrochemical performance, the galvanostatic charge-discharge curves were measured at different current densities with $0.1\text{--}100\text{ A g}^{-1}$ (Fig. 3b). The almost linear and symmetric triangular-type appearances of galvanostatic charge/discharge curves also manifest the

dominant double-layer capacitance behaviors. The discharge curves only show a small voltage drop implying a low equivalent series resistance leading to a large power delivery. The specific capacitances are calculated from the discharge curves of galvanostatic profiles at different current densities (Fig. 3c). At a current density of 0.1 A g^{-1} , the specific capacitance of 301 F g^{-1} was obtained which is superior to some of advanced carbons electrodes such as microporous carbon from carbonization of chemical polymer³³ and the seaweeds,¹⁹ activated carbon from waste newspaper,⁴² sunflower seed shell,⁴³ and well comparable those nitrogen-doping carbons such as human hair-based carbons,²³ and argan seed shells⁴⁴ in aqueous electrolyte system. Compared with these predecessors, the high specific capacitance of BHNC is attributed to not only the reversible pseudocapacitance from limited surface oxygen groups but also the unique hierarchical pore size distribution with a narrow pore size around 0.53 nm matching with the aqueous electrolyte ions as supported by NLDFT analysis. Even at 100 A g^{-1} , a specific capacitance of 192 F g^{-1} retaining 63.8% initial capacitance was maintained, indicating an excellent rate performance, which can result from the high electronic conductivity of 4.5 S cm^{-1} as well as the beehive-like hierarchical nanoporous structures that the wide meso/macropores range from $10\text{-}60 \text{ nm}$ could buffer amount of electrolyte ions and promote the ion transfer into interior pore surface of microporous at high discharge rates leading a high rate performance and high power density.

The CV and galvanostatic charge/discharge of the BHNC-based symmetrical supercapacitors in 6 M KOH were also measured (Fig. S3), which further indicate quick ion/charge transports and dominant electric double-layer capacitor behaviors. The long-term cyclic stability of aqueous symmetrical supercapacitors was evaluated by galvanostatic charge/discharge at several current densities. As shown in Figure 3d, the cell still retains near 100% of initial capacitance after $20,000$ cycles at 1 A g^{-1} evidencing the wonderful stability even at high discharge rates.

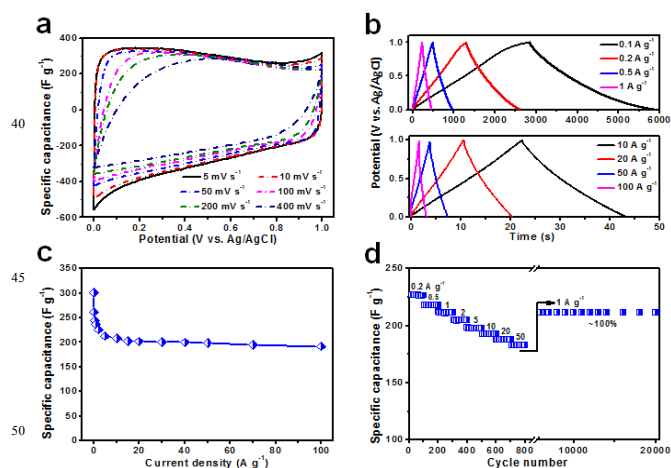


Fig. 3 (a) CV curves, (b) galvanostatic charge-discharge curves and (c) charge/dicharge rate performance of the BHNC-based electrode in three-electrode configuration with 6 M KOH solution as electrolyte. And (d) the long-term cyclic stability at different current densities for the BHNC-based electrode in 6 M KOH .

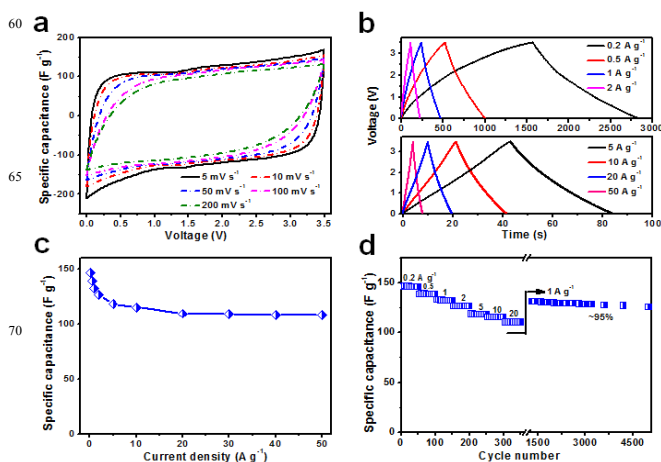


Fig. 4 (a) CV curves, (b) galvanostatic charge-discharge curves, (c) charge/dicharge rate performance and (d) the long-term cyclic stability at different current densities in neat ionic liquid of EMIM TFSI as electrolyte for the BHNC-based electrode.

The practical application of the aqueous supercapacitors is gravely limited due to the low potential window of 1 V leading to the low energy storage. In order to improve the energy density, we therefore measured the non-aqueous symmetrical supercapacitors in a neat ionic liquid electrolyte of EMIM TFSI with a wide potential window of 3.5 V as tested at 60°C . Figure 4a and b show the CV curves with almost rectangular form in all the scan rates and the galvanostatic charge/discharge curves with symmetric triangular-type shapes for the ionic liquid symmetrical supercapacitors, both which indicate a dominant electric double-layer capacitor formation at the interface of electrode and electrolyte. The specific capacitance calculated by the same method for the aqueous system is represented in Figure 4c. The highest specific capacitance of 146 F g^{-1} at 0.2 A g^{-1} was obtained, and 74% capacitance value (*i.e.*, 108 F g^{-1}) was retained at 50 A g^{-1} . These values are superior to that of the reported carbon derived from chemical polymer,³³ leaves,¹¹ and human hair²³ in the organic electrolyte system. After $5,000$ cycles at 1 A g^{-1} the devices show a 95% of initial capacitance (Fig. 4d), due to the degradation of partial electrolyte on the oxygen-containing surface but very limited. Compared with these predecessors in organic/ionic liquid systems, the good electrochemical performances of BHNC result from the high specific surface area and ideal hierarchical pore size distribution with a narrow pore size mainly around 0.53 nm exactly matching with the size of the electrolyte ions (EMIM⁺ of 0.43 nm),^{6,25} leading to a significant enhancement of specific capacitance because the plentiful electrolyte ions are extruded through the micropores and build the ion monolayer inside of micropore under a given potential even at high discharge rates where diffusion limitation is non-significant.^{22, 25-28} Moreover the bottleneck-like meso/macropores could noticeably improve the ion transport kinetics by means of buffering amount of electrolyte and furnishing a convenient ion transfer approach to increase the accessibility of electrolyte ions with microporous areas and decrease the diffusion distances for electrolyte ions to the interior pore wall at high discharge rates.²²

The process is showed in the inset of Figure 6a. In addition, the ionic liquid symmetrical supercapacitors were tested at 60°C when the electrolyte of EMIM TFSI owns high ionic conductivity and transport (melting point of EMIM TFSI is about -15°C), which can effectively alleviate the phenomenon of the ion “traffic jam” in pores of comparable dimensions.^{3, 22} The interconnected porous carbon nanosheet frameworks with high electronic conductivity of BHNC can also be more advantage of ion transport than that of the reported carbon particles²² at high discharge rates. Both of which can lead to an energy and power synergetic outputting property of BHNC-based symmetrical supercapacitors in ionic liquid system.

After eliminating the surface oxygen groups by vacuum annealing at 1000°C, the sample exhibits better rate performance at high discharge current densities due to the higher electronic conductivity of 5.6 S cm⁻¹ than that of BHNC (Fig. S4), but possess almost identical specific capacitance values due to the high annealing temperature possibly resulting in part microstructures collapsed.²⁵ In addition, to further demonstrate that the good match the size of electrolyte ions with pore sizes can enhance the electrode performances, a BHNC-based symmetric supercapacitor using another ionic liquid of BMPY TFSI (BMPY⁺ of 1.1 nm)⁶ as electrolyte was discussed. Figure S5 shows that the cells in BMPY TFSI system exhibits the distorted CV curves and low specific capacitance compared with that of in EMIM TFSI system at the same conditions, due to the larger cationic ion diameter than most of pore sizes of BHNC which leads to inefficient electrolyte ion transport and a high equivalent series resistance.

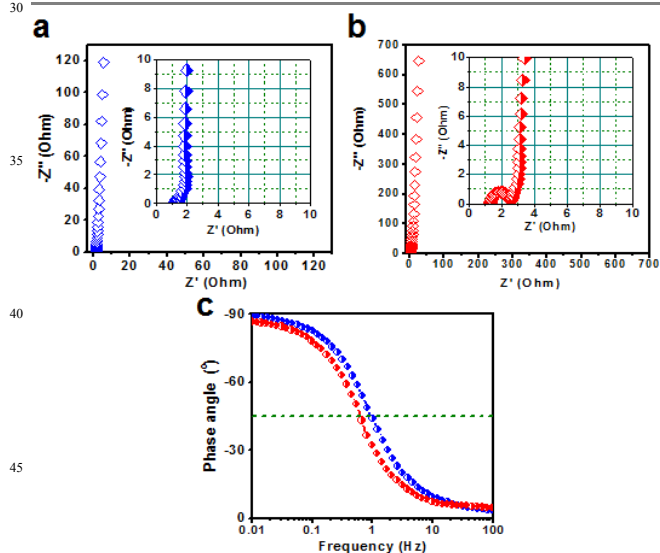


Fig. 5 Nyquist plot for the BHNC-based electrodes (a) in 6 M KOH and (b) in EMIM TFSI, with a magnification for the high-frequency region in the inset (a and b), respectively. And (c) the impedance phase angle versus frequency for the BHNC-based electrodes.

Electrochemical impedance spectroscopy measurement was employed to study the electron/ion transport process and further demonstrated the favorable performance for the BHNC-based electrodes in symmetric supercapacitors. Figure 5a and b show

the Nyquist plots for both aqueous and ionic liquid symmetric supercapacitors. Almost vertical lines normal to the real axis (Z') at a low frequency region distinctly show the ideal capacitance behaviors with very low diffusion resistance R_d .⁴⁵ The data in the magnified high frequency regions are shown in the inset of Figure 5a and b. The Ohmic resistance R_0 of the devices is obtained from the corresponding value of the first intercept of the plots with the real axis, including intrinsic resistance of the active electrode materials, the substrate and electrolyte, and the contact resistance of the electrodes with the external circuit.^{13, 46} The devices own very low R_0 of 1.04 and 1.29 Ω for the aqueous and ionic liquid system, respectively. The small semicircles in the high to medium region in the inset of Figure 5a and b reflect the low charge transfer resistance R_{ct} . Low R_{ct} and the short Warburg region at the 45° sloped curves effected by the porosity, wettability and thickness of electrode materials,^{23, 47} indicate the efficient charge transfer process in the BHNC-based electrodes. The equivalent series resistance R_{est} is 1.89 and 3.09 Ω for the aqueous and ionic liquid system, respectively, further suggesting the excellent conducting performance of the samples. Importantly, these values are considerably lower than that of the recently reported carbons by direct pyrolysis of chemical polymer³³ and dead leaves¹¹.

Figure 5c shows the Bode plots of the frequency response. The characteristic frequency f_0 for a phase angle of -45° is 0.95 and 0.61 Hz for the aqueous and ionic liquid system, respectively. The corresponding relaxation time constant τ_0 ($1/f_0$) is 1.05 (aqueous) and 1.64 s (ionic liquid), which are well comparable with that of the activated graphene (1.67 s),⁴⁸ and obviously lower than that of the commercial active carbon (10-100 s),^{8, 25} metal carbide-derived carbon^{29, 30} and advanced microporous carbon from the carbonation of chemical polymers.^{10, 33} The fast frequency response further confirms the superiority of the beehive-like nanoporous carbon as supercapacitors electrode for high discharge rates with good capacitance retention and high power delivery.

In order to assess the overall energy and power characteristics of the BHNC-based symmetric supercapacitors, the Ragone plots are given in Figure 6a based on the mass of active electrode materials. The BHNC-based aqueous symmetric supercapacitors exhibit a high energy density of 9.5 Wh kg⁻¹ at gravimetric power density of 25 W kg⁻¹, whereas the energy density still remains 6.1 Wh kg⁻¹ at high power density of 26,000 W kg⁻¹. In ionic liquid system, the energy density is increased to 58.6 Wh kg⁻¹ at power density of 166 W kg⁻¹ due to the potential window extended to 3.5 V, more importantly 73.9% energy density of 43.3 Wh kg⁻¹ is remained at extractable power density of 42,000 W kg⁻¹, which is better than that of the reported microporous carbide-derived carbon (23.8 Wh kg⁻¹),²⁹ hierarchical porous graphitic carbon (22.9 Wh kg⁻¹)⁴⁹ and interconnected carbon nanosheets (40 Wh kg⁻¹)⁶ based on the active electrode materials. These results indicate that BHNC-based supercapacitors can deliver a great mass of energy-power densities at the same time owing to ultrafast electron/ion transports, suggesting the increase of power density without obviously compromising the value of energy density. In addition, we compare the energy-power characteristics of BHNC-based electrodes with those of state-of-the-art porous carbons synthesized from natural biomass^{6, 23, 27} and chemical

polymer,^{10, 33, 50} metal carbide-derived carbon,²⁹ carbon nanotube,⁵¹ graphene^{12, 13, 52} and other advanced carbons^{49, 53-55} based on the total active mass of both electrodes (Fig. 6b). The BHNC-based electrodes locate among the best energy-power characteristics in ever reported for carbon-based supercapacitors. In order to extrapolate the practical energy and power densities of the packaged cells in ionic liquid system, the normalized values based on total cell mass is obtained from 1/4 of the performance values based on active electrode materials, according to the active electrode materials representing about 30% weight ratio of whole mass of all cell components.^{6, 14, 48, 52, 56, 57} Figure 6c shows the Ragone plots of BHNC-based packaged cell in ionic liquid system based on the total devices compared with commercial electronic energy storage devices.¹ The normalized energy densities of the assumed packaged cell are expected for about 10.8~14.6 Wh kg⁻¹ which are about 2~3 higher than that of the commercial AC-based supercapacitors.^{6, 10} The normalized maximum power density of the devices is about 10 kW kg⁻¹, suggesting that the devices could recharge completely in only 3.6 s. These results show that BHNC-based packaged cell can successfully cross the performance gap between the electrochemical capacitor and Ni-metal hydride (NiH) batteries.

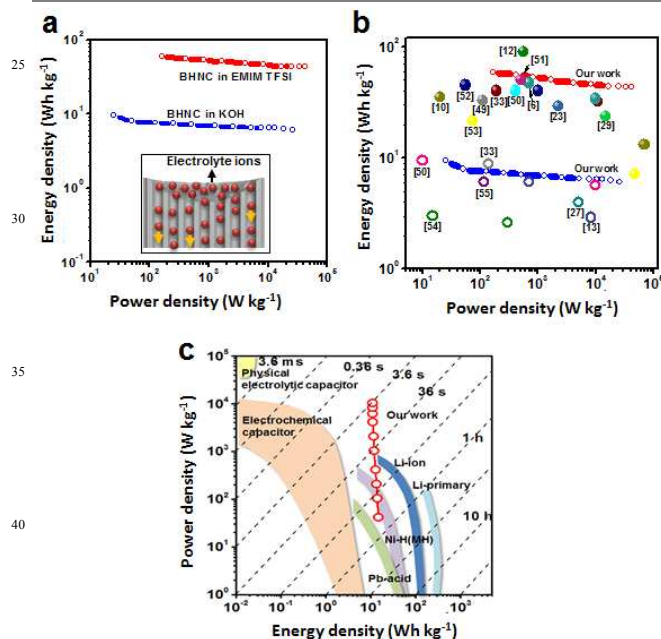


Fig. 6 (a) Ragone plots for the BHNC-based symmetrical supercapacitors in different electrolytes (insert of (a) is the schematic representation of the possible electrolyte ions transport mechanism of BHNC-based electrodes), and (b) performance comparison of the BHNC versus literature reported values for state-of-the-art carbon materials (hollow: aqueous electrolyte, and solid: non-aqueous electrolyte) based on the total active mass of both electrodes. And (c) performance comparison of BHNC-based devices with the commercial electronic energy storage devices (Data from ref. 1).

The prominent performances such as high specific capacitance and rate capability, excellent long-term cyclic stability, low equivalent series resistance and fast frequency response of the as-

prepared BHNC-based electrodes are attributed to the unique beehive-like nanoporous structures on the interconnected carbon nanosheet frameworks with the high specific surface area and hierarchical pore size distributions. In order to further confirm the key role of the beehive-like nanoporous structures on the interconnected carbon nanosheet frameworks with hierarchical pore size distribution to the electrochemical application, a control sample with only narrow pore size distribution of about 0.54 nm (96% micropore volume) was prepared. The corresponding data is shown in Figure S6. It can be clearly seen that the control sample displays significant distorted CV curves at high scan rates and a lower capacitance response compared with BHNC both in aqueous and ionic liquid systems under the same conditions. These results are attributed to that the control sample only possesses a narrow micropore system without the meso/macropore system to buffer vast electrolyte ions and thus owns an inefficiently ion transfer process at high scan rates. In order to demonstrate the effective of post-synthesis vacuum annealing, the control sample without the treatment of vacuum annealing at 800°C exhibits lower specific capacitance and larger equivalent series resistance than that of BHNC in either electrolyte due to low electronic conductivity (Fig. S7). It should be noted that the activation parameters (mass ratio of KOH/carbon, activation temperature and time) of BHNC were optimized (Fig. S8), which are attributed to the comprehensive effect of complex activation reactions and district carbon precursor of bamboo fibers.⁵⁸⁻⁶⁰

Conclusions

A novel beehive-like hierarchical nanoporous carbon BHNC has been successfully prepared from an industrial waste of bamboo-based bioactive-substance extraction residues, using a low-cost and environmentally benign bio-inspired approach. The BHNC sample possesses a unique beehive-like hierarchical nanoporous structure on the interconnected carbon nanosheet frameworks and good electronic conductivity differed from other reported biomass-derived carbons and chemical polymer-derived carbons, which are attributed to the unique natural hierarchical texture structures and high cellulose composition of bamboo-based precursor as well as the distinct synthesis approach. The BHNC exhibits the prominent performances as supercapacitor electrodes (high specific capacitances, rate capabilities, excellent long-term cyclic stabilities, low equivalent series resistances and fast frequency responses) both in aqueous and ionic liquid systems because of the unique beehive-like nanoporous structures facilitating ultrafast electron/ion transport. Furthermore, On the Ragone chart the BHNC-based supercapacitors possess high energy-power synergetic outputting property among the best ever reported for carbon-based supercapacitors. The packaged BHNC-based devices in ionic liquid system can cross the performance gap between the electrochemical capacitor and Ni-metal hydride batteries. These promising results reveal a green value-added secondary-utilization window for biomass-based industrial byproducts to produce advanced carbons as high performance energy storage electrode materials.

Acknowledgements

This work is supported by National Basic Research Programs of

China (973 Programs, No.2011CB935700 and 2014CB931800), Chinese Aeronautic Project (No. 2013ZF51069) and Chinese National Science Foundation (No. U0734002).

Notes and references

⁵ ^a Key Laboratory of Bio-inspired Smart Interfacial Science and Technology of Ministry of Education, Beijing Key Laboratory of Bio-inspired Energy Materials and Devices, School of Chemistry and Environment, Beihang University, Beijing100191, China. Email: qmgao@buaa.edu.cn.

¹⁰ † Electronic Supplementary Information (ESI) available: [Fig. S1-8]. See DOI: 10.1039/b000000x/

1. P. Simon and Y. Gogotsi, *Nat. Mater.*, 2008, **7**, 845-854.
2. H. Jiang, P. S. Lee and C. Li, *Energy Environ. Sci.*, 2013, **6**, 41-53.
3. L. Li and A. Manthiram, *Adv. Energy Mater.*, 2014, **4**, DOI: 10.1002/aenm.201301795.
4. L. Li, S.-H. Chai, S. Dai and A. Manthiram, *Energy Environ. Sci.*, 2014, **7**, 2630-2636.
5. D. Higgins, Z. Chen, D. U. Lee and Z. Chen, *J. Mater. Chem. A*, 2013, **1**, 2639-2645.
6. H. Wang, Z. Xu, A. Kohandehghan, Z. Li, K. Cui, X. Tan, T. J. Stephenson, C. K. King'ondeu, C. M. Holt, B. C. Olsen, J. K. Tak, D. Harfield, A. O. Anyia and D. Mitlin, *ACS Nano*, 2013, **7**, 5131-5141.
7. Z. S. Wu, K. Parvez, X. Feng and K. Müllen, *Nat. Commun.*, 2013, **4**, 2487.
8. M. F. El-Kady, V. Strong, S. Dubin and R. B. Kaner, *Science*, 2012, **335**, 1326-1330.
9. S. Kondrat, C. R. Perez, V. Presser, Y. Gogotsi and A. A. Kornyshev, *Energy Environ. Sci.*, 2012, **5**, 6474-6479.
10. M. Sevilla and A. B. Fuertes, *ACS Nano*, 2014, **8**, 5069-5078.
11. M. Biswal, A. Banerjee, M. Deo and S. Ogale, *Energy Environ. Sci.*, 2013, **6**, 1249-1259.
12. C. Liu, Z. Yu, D. Neff, A. Zhamu and B. Z. Jang, *Nano Lett.*, 2010, **10**, 4863-4868.
13. J. Luo, H. D. Jang and J. Huang, *ACS Nano*, 2013, **7**, 1464-1471.
14. Y. Zhu, S. Murali, M. D. Stoller, K. Ganesh, W. Cai, P. J. Ferreira, A. Pirkle, R. M. Wallace, K. A. Cychosz, M. Thommes, D. Su, E. A. Stach and R. S. Ruoff, *Science*, 2011, **332**, 1537-1541.
15. X. Yang, C. Cheng, Y. Wang, L. Qiu and D. Li, *Science*, 2013, **341**, 534-537.
16. Y. Fang, B. Luo, Y. Jia, X. Li, B. Wang, Q. Song, F. Kang and L. Zhi, *Adv. Mater.*, 2012, **24**, 6348-6355.
17. T. Yu, J. Jiang, J. Zhu, W. Ai, Z. Fan, H. Zhang, J. Liu, X. Shen and C. Zou, *Energy Environ. Sci.*, 2014, **7**, 2670-2679.
18. E. Raymundo-Pinero, F. Leroux and F. Beguin, *Adv. Mater.*, 2006, **18**, 1877-1882.
19. E. Raymundo-Pinero, M. Cadek and F. Beguin, *Adv. Funct. Mater.*, 2009, **19**, 1032-1039.
20. Z. Li, Z. W. Xu, H. L. Wang, J. Ding, B. Zahiri, C. M. B. Holt, X. H. Tan and D. Mitlin, *Energy Environ. Sci.*, 2014, **7**, 1708-1718.
21. Z. Li, Z. Xu, X. Tan, H. Wang, C. M. B. Holt, T. Stephenson, B. C. Olsen and D. Mitlin, *Energy Environ. Sci.*, 2013, **6**, 871-878.
22. Z. Li, L. Zhang, B. S. Amirkhiz, X. Tan, Z. Xu, H. Wang, B. C. Olsen, C. M. B. Holt and D. Mitlin, *Adv. Energy Mater.*, 2012, **2**, 431-437.
23. W. Qian, F. Sun, Y. Xu, L. Qiu, C. Liu, S. Wang and F. Yan, *Energy Environ. Sci.*, 2014, **7**, 379-386.
24. J. Xu, Q. Gao, Y. Zhang, Y. Tan, W. Tian, L. Zhu and L. Jiang, *Sci. Rep.*, 2014, **4**, 5545.
25. L. Wei, M. Sevilla, A. B. Fuertes, R. Mokaya and G. Yushin, *Adv. Energy Mater.*, 2011, **1**, 356-361.
26. L. Zhang, F. Zhang, X. Yang, K. Leng, Y. Huang and Y. S. Chen, *Small*, 2013, **9**, 1342-1347.
27. C. Falco, J. M. Sieben, N. Brun, M. Sevilla, T. van der Maelen, E. Morallon, D. Cazorla-Amoros and M. M. Titirici, *ChemSusChem*, 2013, **6**, 374-382.
28. D. Weingarh, M. Zeiger, N. Jäckel, M. Aslan, G. Feng and V. Presser, *Adv. Energy Mater.*, 2014, **4**, DOI: 10.1002/aenm.201400316.
29. J. Chmiola, G. Yushin, Y. Gogotsi, C. Portet, P. Simon and P.-L. Taberna, *Science*, 2006, **313**, 1760-1763.
30. C. Largeot, C. Portet, J. Chmiola, P.-L. Taberna, Y. Gogotsi and P. Simon, *J. Am. Chem. Soc.*, 2008, **130**, 2730-2731.
31. G. Yushin, R. Dash, J. Jagiello, J. E. Fischer and Y. Gogotsi, *Adv. Funct. Mater.*, 2006, **16**, 2288-2293.
32. A. Kajdos, A. Kvit, F. Jones, J. Jagiello and G. Yushin, *J. Am. Chem. Soc.*, 2010, **132**, 3252-3253.
33. P. Dhanya, V. Aravindan, M. Srinivasan and S. Ogale, *Energy Environ. Sci.*, 2014, **7**, 728-735.
34. A. Tanaka, Q. C. Zhu, H. Tan, H. Horiba, K. Ohnuki, Y. Mori, R. Yamauchi, H. Ishikawa, A. Iwamoto, H. Kawahara and K. Shimizu, *Molecules*, 2014, **19**, 8238-8260.
35. D. Wu, J. Chen, B. Lu, L. Xiong, Y. He and Y. Zhang, *Food Chem.*, 2012, **135**, 2147-2156.
36. H. Zhu, X. Wang, F. Yang and X. Yang, *Adv. Mater.*, 2011, **23**, 2745-2748.
37. N. Shimodaira and A. Masui, *J. Appl. Phys.*, 2002, **92**, 902-909.
38. I. K. Moon, J. Lee, R. S. Ruoff and H. Lee, *Nat. Commun.*, 2010, **1**, 73.
39. B. Xu, S. Yue, Z. Sui, X. Zhang, S. Hou, G. Cao and Y. Yang, *Energy Environ. Sci.*, 2011, **4**, 2826-2830.
40. H. Zhu, X. L. Wang, X. X. Liu and X. R. Yang, *Adv. Mater.*, 2012, **24**, 6524-6529.
41. L. Hao, X. Li and L. Zhi, *Adv. Mater.*, 2013, **25**, 3899-3904.
42. D. Kalpana, S. H. Cho, S. B. Lee, Y. S. Lee, R. Misra and N. G. Renganathan, *J. Power Sources*, 2009, **190**, 587-591.
43. X. Li, W. Xing, S. Zhuo, J. Zhou, F. Li, S.-Z. Qiao and G.-Q. Lu, *Bioresource Technol.*, 2011, **102**, 1118-1123.
44. A. Elmouwahidi, Z. Zapata-Benabithé, F. Carrasco-Marín and C. Moreno-Castilla, *Bioresource Technol.*, 2012, **111**, 185-190.
45. E. Frackowiak and F. Béguin, *Carbon*, 2001, **39**, 937-950.
46. B. G. Choi, M. Yang, W. H. Hong, J. W. Choi and Y. S. Huh, *ACS Nano*, 2012, **6**, 4020-4028.
47. Z. Lei, Z. Liu, H. Wang, X. Sun, L. Lu and X. Zhao, *J. Mater. Chem. A*, 2013, **1**, 2313-2321.
48. T. Kim, G. Jung, S. Yoo, K. S. Suh and R. S. Ruoff, *ACS Nano*, 2013, **7**, 6899-6905.
49. D.-W. Wang, F. Li, M. Liu, G. Q. Lu and H.-M. Cheng, *Angew. Chem. Int. Ed.*, 2008, **120**, 379-382.
50. L. Qie, W. M. Chen, H. H. Xu, X. Q. Xiong, Y. Jiang, F. Zou, X. L. Hu, Y. Xin, Z. L. Zhang and Y. H. Huang, *Energy Environ. Sci.*, 2013, **6**, 2497-2504.
51. W. Lu, R. Hartman, L. Qu and L. Dai, *J. Phys. Chem. Lett.*, 2011, **2**, 655-660.
52. F. Zhang, T. F. Zhang, X. Yang, L. Zhang, K. Leng, Y. Huang and Y. S. Chen, *Energy Environ. Sci.*, 2013, **6**, 1623-1632.
53. Z. Xu, Z. Li, C. M. B. Holt, X. Tan, H. Wang, B. S. Amirkhiz, T. Stephenson and D. Mitlin, *J. Phys. Chem. Lett.*, 2012, **3**, 2928-2933.
54. T. Morishita, Y. Soneda, T. Tsumura and M. Inagaki, *Carbon*, 2006, **44**, 2360-2367.
55. W. Xing, S. Z. Qiao, R. G. Ding, F. Li, G. Q. Lu, Z. F. Yan and H. M. Cheng, *Carbon*, 2006, **44**, 216-224.
56. Y. Gogotsi and P. Simon, *Science*, 2011, **334**, 917-918.
57. M. D. Stoller and R. S. Ruoff, *Energy Environ. Sci.*, 2010, **3**, 1294-1301.
58. M. Sevilla and R. Mokaya, *Energy Environ. Sci.*, 2014, **7**, 125-1280.
59. J. Wang and S. Kaskel, *J. Mater. Chem.*, 2012, **22**, 23710-23725.
60. M. Sevilla, A. B. Fuertes and R. Mokaya, *Energy Environ. Sci.*, 2011, **4**, 1400-1410.

ToC figure

